Journal of the European Ceramic Society 44 (2024) 2982–2988

Contents lists available at ScienceDirect

Journal of the European Ceramic Society

journal homepage: www.elsevier.com/locate/jeurceramsoc

Effect of B-site doping on the thermoelectric performances of $Ca_{0.97}Y_{0.01}La_{0.01}Yb_{0.01}Mn_{1\text{-}2x}Nb_xMo_xO_3$ thermoelectric ceramics

P. Amirkhizi [a,*], M.A. Torres [b], O.J. Dura [c], A. Sotelo [b], M.A. Madre [b], A. Kovalevsky [a], Sh. Rasekh [a]

[a] *Department of Materials and Ceramic Engineering, CICECO-Aveiro Institute of Materials, University of Aveiro, 3810-193 Aveiro, Portugal*
[b] *INMA (CSIC-Universidad de Zaragoza), Mª de Luna, 3. 50018 Zaragoza, Spain*
[c] *Applied Physics Department, University of Castilla-La Mancha, 13071 Ciudad Real, Spain*

ARTICLE INFO

Keywords:
Thermoelectric oxide
Ceramics
Electrical properties
Thermal conductivity

ABSTRACT

A-, and B-site multiple-doped $Ca_{0.97}Y_{0.01}La_{0.01}Yb_{0.01}Mn_{1-2x}Nb_xMo_xO_3$ was studied for improving its thermoelectric thermoelectric performance. Samples were prepared from planetary milled precursors and sintered at 1310ºC for 12 h. XRD showed that sintered samples are nearly single phase, with small amounts of $CaMn_2O_4$. SEM analysis revealed that grain size decreases with Nb and Mo content, leading to lowered electrical resistivity, reaching 6.1 mΩ cm at 800ºC in $x = 0.03$ samples, 60% lower than that of pristine samples. The highest Seebeck coefficient for doped samples has been obtained for $x = 0.005$, 210μV/K at 800ºC. A high power factor (0.46 mW/K^2 m at 800ºC) has been reached for $x = 0.01$ samples. However, thermal conductivity did not significantly vary with composition, leading to ZT~0.27 at 800ºC for $x = 0.005$ samples, among the best reported in the literature. These results suggest that multi-doping approach opens new paths for integrating calcium manganite-based materials in thermoelectric modules for power generation at high temperatures.

1. Introduction

Nowadays, one of the world's most important problems is the need to reduce the use of fossil fuels to fight against global warming due to the massive emission of greenhouse gases when using these fuels. This requires the massive use renewable energy sources, such as photovoltaic, wind power, etc. However, the renewable energy production today is not sufficient to satisfy the world's energetic requirements. Another notable limitation for using renewable energies is their daily and seasonal intermittency. As a consequence, even if their need should decrease, fossil fuels still have to be used to achieve the required energy production. On the other hand, it is well known that the classical energy conversion systems possess relatively low efficiency, wasting about 60% of the initial energy in the form of heat. In this regard, the thermoelectric (TE) power generation is one of the promising ways to harvest waste heat produced in the processes associated with fossil fuels, or from renewable sources, and converting it into usable electrical energy [1,2]. Thermoelectric technology is very reliable and has a long service life, as it has been used in many fields, e.g., NASA's space missions Voyager 1 & 2 launched in 1977 which are still working. Nevertheless, to make thermoelectric technology feasible, it is necessary to develop materials with high conversion efficiency to supply competitive devices. The efficiency is usually evaluated through the so-called figure of merit ZT, defined as $TS^2/\rho\kappa$ (T is absolute temperature, S Seebeck coefficient, ρ electrical resistivity, and κ thermal conductivity) [3].

At present, it is possible to find commercial TE modules, which are built using semiconducting or intermetallic TE legs. However, these materials usually comprise heavy and toxic elements, and can only operate at relatively low temperatures to avoid their degradation. Moreover, they often contain elements that are scarce in the earth crust and expensive [4,5]. Nevertheless, the discovery of promising TE properties in ceramic oxides has allowed finding materials able to work at high temperatures, and also composed of cheaper and more abundant elements [6]. Among these compounds, the most promising families to be used in TE modules are $Ca_3Co_4O_9$ as p-type component [7], and $CaMnO_3$ as n-type component [8]. It should be mentioned that these materials still possess relatively low TE performances, being typically higher for the p-type compounds. The pristine $CaMnO_3$ shows very low performances due to its very low charge carrier concentration, leading to high electrical resistivity. Consequently, it has to be electronically

---

* Corresponding author.
E-mail address: parisa.amirkhizi@ua.pt (P. Amirkhizi).

https://doi.org/10.1016/j.jeurceramsoc.2023.12.067
Received 20 October 2023; Received in revised form 15 December 2023; Accepted 17 December 2023

doped to enhance the charge carrier concentration towards reasonable TE performance. This family of materials presents an orthorhombic perovskite structure [9], and the charge carriers can be generated by substituting Ca with rare earth elements [10,11], Mn by transition metals [12,13], or both substitutions at the same time [14,15], to obtain a significant increase in TE performance. Another factor having a drastic influence on the final properties of the bulk sintered materials is the starting particle sizes, which can modify their reactivity and, therefore, the final density of thermoelectric ceramics [16–18].

When evaluating the results reported in the literature, it can be found that using more than one substituting cation allows a notable increase of the thermoelectric performances [19]. Moreover, recent work has shown that triple doping in the Ca site leads to an enhancement of ZT by improving the phonon scattering [20]. It is important to notice that the approach of simultaneous doping/substitution in ceramics shares a conceptual parallel with high-entropy ceramics, as both strategies involve the compositional complexity to design the material properties [21]. While simultaneous doping/substitution strives to tailor the lattice and electronic structure, high-entropy ceramics rely on the entropy stabilisation mechanism, but both explore a compositional space to derive novel and enhanced properties. This work focuses on increasing the TE performance of $CaMnO_3$ by using various dopants in the A and B sites of the crystal structure and relying on the distortion of the crystal structure. The structural and microstructural evolution produced by these involved substitutions has been studied and related to the variation of thermoelectric properties.

2. Experimental

All the $Ca_{0.97}Y_{0.01}La_{0.01}Yb_{0.01}Mn_{1-2x}Nb_xMo_xO_3$ ($0 \leq x \leq 0.03$) compounds were obtained through their initial precursors, $CaCO_3$ (≥ 99%, Aldrich), Y_2O_3 (99.99%, Aldrich), La_2O_3 (≥ 99.9%, Aldrich), Yb_2O_3 (99.9%, Aldrich), Mn_2O_3 (99.9%, Aldrich), Nb_2O_5 (99.5%, Alfa Aesar), and MoO_3 (99 + %, Aldrich). They were weighed and mixed in stoichiometric proportions, and then they were milled in a planetary ball mill at 400 rpm for 4 h in water medium. The slurry was then subjected to IR radiation until total water evaporation; the dry mixture was manually milled to obtain a fine and homogeneous powder, which was subsequently calcined at 950 ºC for 12 h, and 1050 ºC for 12 h under air atmosphere, with an intermediate manual milling. For these treatments, 5 ºC/min, and 10 ºC/min heating and cooling rates, respectively, were used. Finally, the powders were cold uniaxially pressed in the form of pellets ($3 \times 3 \times 15$ mm^3) under 400 MPa, and sintered at 1310 ºC for 12 h under air, with 3 ºC/min heating rate, and cooled to room temperature at 5 ºC/min.

Powder X-ray diffraction (XRD) was performed in a Rigaku Ru300 in the range 10–80 º working at 40 KV and 80 mA, with 0.03 º step and 3 s/step, to determine the phases present in the samples. The absolute density has been measured by Archimedes' method using at least three samples for each composition, and relative density has been calculated for all samples taking 4.705 g/cm^3 as the theoretical density [17]. The microstructural evolution was studied on the samples surfaces with a Field Emission Scanning Electron Microscope (FESEM, Zeiss Merlin) equipment; their elemental composition was determined by energy dispersive spectrometry (EDS). The grain sizes were estimated for sintered materials using the line intercept method [22].

Both Seebeck coefficient and electrical resistivity of samples were simultaneously measured using the standard DC four-probe technique in steady state mode, in a LSR-3 system (Linseis GmbH) under Helium atmosphere, between 50 and 800 ºC, using 10 ºC/min heating rate. Total thermal conductivity (κ) was determined using the expression $\kappa = \alpha C_p d$, where α is thermal diffusivity, C_p specific heat, and d density of the sample. α has been determined using a laser-flash system (Linseis LFA 1000) between 50 and 800 ºC, with 10 ºC/min heating rate, in the same direction as in the case of electrical characterization, while C_p has been calculated using Dulong-Petit law. Finally, with the electrical and thermal data, the ZT evolution with temperature was calculated and compared with the results reported in the literature for this family of compounds.

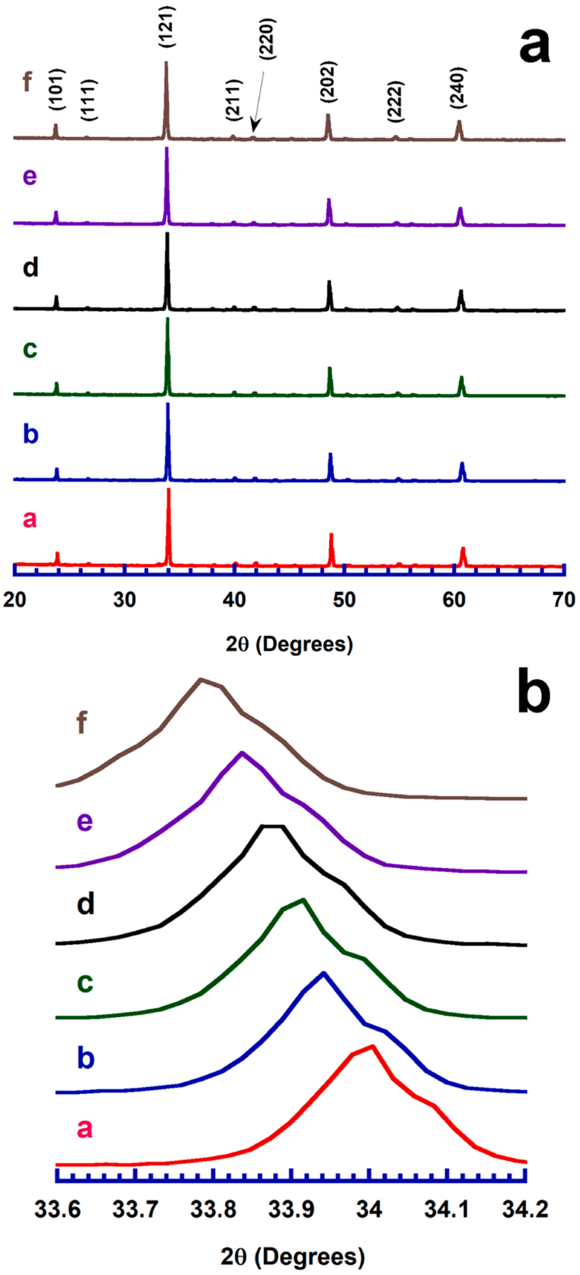

Fig. 1. a) Powder XRD patterns recorded after sintering at 1310 ºC for 12 h; and b) Representative XRD peak at 34 degrees showing the shift of this peak for $Ca_{0.97}Y_{0.01}La_{0.01}Yb_{0.01}Mn_{1-2x}Nb_xMo_xO_3$ samples, with x = a) 0.0; b) 0.005; c) 0.010; d) 0.015; e) 0.020; and f) 0.030.

3. Results and discussion

The powder XRD patterns are presented (from 20 to 70 degrees for the sake of clarity) in Fig. 1a for all samples. As it can be easily observed in the graph, the most intense peaks correspond to the $CaMnO_3$ phase with a Pnma space group (indicated in the plot through their diffraction planes), in agreement with previously reported data [23,24]. Moreover, the peaks of the main phase shift to lower angles when the amount of Nb, and Mo is increased, as reflected in Fig. 1b, where an enlarged view of the 34 º peak for all samples is displayed. In order to evaluate the

Table 1
Lattice parameters as a function of the dopant content, as well as the wt% of $CaMn_2O_4$ secondary phase, obtained from the XRD data.

Composition $Ca_{0.97}Y_{0.01}La_{0.01}Yb_{0.01}Mn_{1-2x}Nb_xMo_xO_3$	a (Å)	b (Å)	c (Å)	wt% $CaMn_2O_4$
x = 0	5.2890 (8)	7.4639 (4)	5.2727 (7)	6.9
x = 0.005	5.2942 (5)	7.4706 (4)	5.2786 (5)	4.1
x = 0.010	5.2994 (5)	7.4765 (9)	5.2829 (5)	4.5
x = 0.015	5.3044 (5)	7.4815 (4)	5.2863 (5)	4.4
x = 0.020	5.3106 (3)	7.4870 (0)	5.2903 (3)	4.4
x = 0.030	5.3222 (3)	7.4989 (2)	5.2988 (3)	5.7

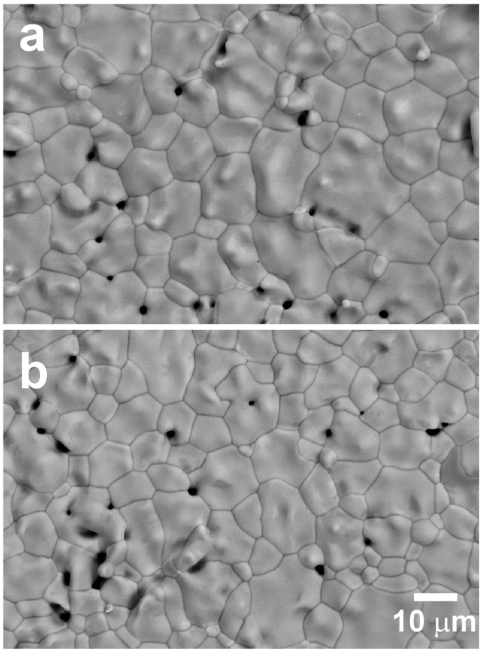

Fig. 2. Representative SEM micrographs performed on the surfaces of sintered $Ca_{0.97}Y_{0.01}La_{0.01}Yb_{0.01}Mn_{1-2x}Nb_xMo_xO_3$ samples, for x = a) 0.0; and b) 0.030.

Table 2
Mean grain sizes of samples, together with their standard error, mean densities with their standard error, and their relative density.

Composition $Ca_{0.97}Y_{0.01}La_{0.01}Yb_{0.01}Mn_{1-2x}Nb_xMo_xO_3$	Mean grain size (μm)	Std. error	Density (g/cm^3)	Std. error	Relative density (%)
x = 0	8.07	0.37	4.29	0.04	91
x = 0.005	8.10	0.20	4.27	0.09	91
x = 0.010	7.52	0.11	4.33	0.04	92
x = 0.015	7.22	0.11	4.33	0.02	92
x = 0.020	7.03	0.13	4.33	0.06	92
x = 0.030	6.76	0.17	4.41	0.02	94

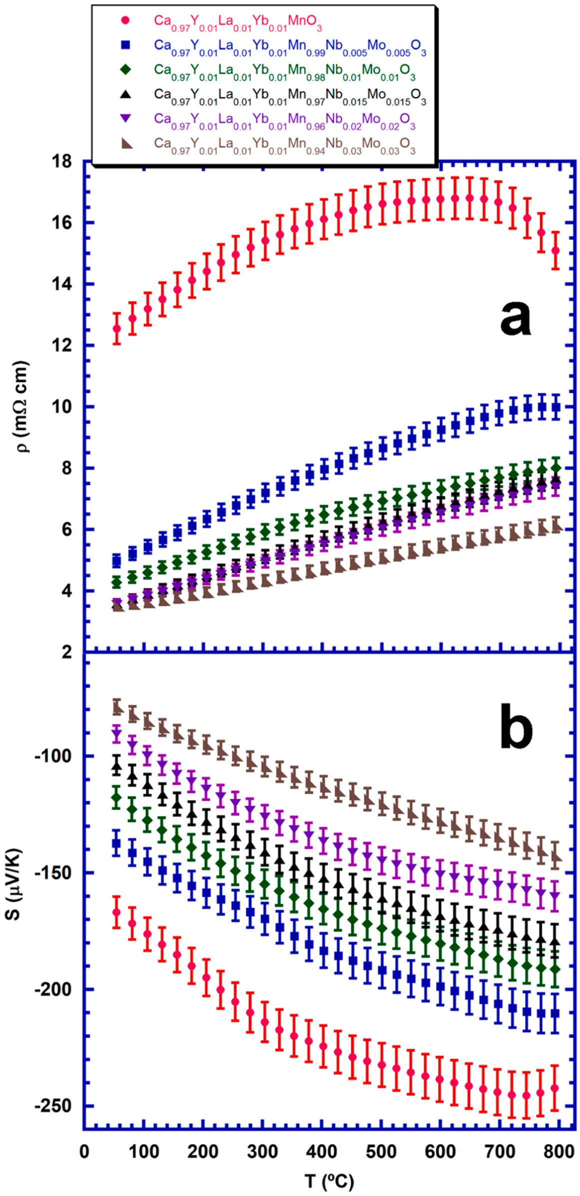

Fig. 3. Evolution with temperature of a) electrical resistivity; and b) Seebeck coefficient, together with their errors, for all samples.

changes in the lattice parameters, and the amount and type of secondary phases, the data were refined using Fullprof Suite software distributed by Roisnel et al. [25].

The obtained results are summarized in Table 1, where the variation of lattice parameters, and the wt% of $CaMn_2O_4$ secondary phase, as a function of Nb, and Mo content, are shown. The lattice parameters monotonically increase with the amount of dopants, due to the higher ionic radii and the increase of oxygen content in the structure provided by the higher oxidation state of Mo, and Nb, when compared to that of Mn. Moreover, the doped samples present slightly lower content of $CaMn_2O_4$ phase, when they are compared to the pristine sample. On the other hand, the amount of secondary phase in the doped samples is close to each other, being slightly higher for the highest doped one.

In Fig. 2, representative SEM micrographs obtained for the surfaces of all samples after sintering, are shown. When observing these micrographs, grain sizes appear to decrease when the amount of dopant increases. In order to evaluate the variation of grain size as a function of the Nb, and Mo content, the line-intercept method has been applied to several micrographs of each sample, and the mean values are presented in Table 2. As it can be easily seen in these data, grain sizes are essentially not modified for the lowest doping (x = 0.005) and decrease monotonically for higher doping, confirming the conclusions drawn from visual observations of the micrographs. In fact, the microstructural refinement is often observed for doped ceramic materials and it is attributed to the combined effect of the thermodynamically reduced

Table 3
Thermoelectric parameters, electrical resistivity, Seebeck coefficient, power factor, thermal conductivity, and ZT, at around 800 °C for the $CaMnO_3$ family reported in literature.

Composition	ρ (mΩ cm)	|S| (μV/K)	PF (mW/K^{2}m)	κ (W/K m)	ZT	Reference
$Ca_{0.9}Dy_{0.1}MnO_3$	7.0	105	0.18	1.8	0.075	[9]
$Ca_{0.95}La_{0.05}MnO_3$	13.9	265	0.50	2.6	0.19	[13]
$CaMn_{0.95}Mo_{0.05}O_3$	16.3	263	0.42	3.1	0.14	[13]
$Ca_{0.96}Bi_{0.04}Mn_{0.96}V_{0.04}O_3$	8.3	150	0.27	1.5	0.21	[14]
$Ca_{0.96}Gd_{0.04}MnO_3$	9.1	180	0.36	2.7	0.13	[17]
$Ca_{0.96}Dy_{0.02}Yb_{0.02}MnO_3$	9.0	175	0.36	1.5	0.27	[19]
$CaMnO_3$	26	320	0.39	-	-	[35]
$Ca_{0.9}Yb_{0.1}MnO_3$	10	140	0.17	-	-	[36]
$Ca_{0.9}Dy_{0.05}Na_{0.05}MnO_3$	22	220	0.22	-	-	[37]
$Ca_{0.88}Pr_{0.08}Sr_{0.04}MnO_3$	6.3	150	0.37	1.7	0.20	[38]
$Ca_{0.9}Bi_{0.1}MnO_3$	5.6	120	0.28	3.5	0.09	[39]
$Ca_{0.96}Bi_{0.04}MnO_3$	11.5	177	0.27	3.1	0.09	[40]
$Ca_{0.96}Dy_{0.02}Yb_{0.02}MnO_3$	19	195	0.20	1.1	0.18	[41]
$Ca_{0.9}Dy_{0.1}MnO_3$	7.0	150	0.35	1.8	0.20	[42]
$Ca_{0.98}Dy_{0.02}MnO_3$	30	250	0.22	1.75	0.07	[43]
$CaMnO_3$/10% $CaMn_2O_4$	13.3	150	0.20	2.6	0.08	[44]
$Ca_{0.7}Sr_{0.3}Mn_{0.96}Yb_{0.04}O_3$	7.5	120	0.18	2.0	0.09	[45]
$Ca_{0.98}La_{0.02}MnO_3$	11.1	215	0.18	2.9	0.06	[46]
$CaMnO_3$	100	225	0.50	16.6	0.03	[47]
$CaMn_{0.98}Nb_{0.02}O_3$	31.8	247	0.19	0.8	0.32	[48]
$Ca_{0.97}Pr_{0.03}MnCu_{0.04}O_3$	8.3	214	0.55	1.5	0.44	[49]

grain-boundary energy and kinetically reduced grain boundary mobility [26].

Another feature that can be observed in Fig. 2 is the different amount of porosity found in these samples, which seems to increase with the doping content. However, when observing all samples, it is increased up to $x = 0.015$, slightly decreasing for higher doping. In order to confirm this evolution, Archimedes' method was applied for several samples for each composition, and the results are also compared in Table 2. These data clearly point out a negligible modification of density with the composition, except for the highest doped samples ($x = 0.030$). This evolution can be explained by the existence of two opposite trends: On one hand, the porosity due to the dopants content increases, which indeed reduces density; on the other hand, the effect of the higher atomic weight of dopants, which increases density even though the slight increase of the lattice parameters also takes place. In any case, the values presented in Table 2 point out to very good densification during the sintering, obtaining relative densities between 91–94% of the theoretical density of $CaMnO_3$ [17]. Moreover, these values are higher than the typically reported for materials prepared through solid-state sintering (66–86%) [27–29]. It should be noted that, although the $CaMn_2O_4$ secondary phase was identified by XRD, EDS analysis performed for the different samples did not reveal grains with manganese excess, which can be assigned to $CaMn_2O_4$ composition. This observation is aligned with previously published results, which showed that this phase appears inside the $CaMnO_3$ grains [20], while only producing very small compositional modifications hardly detectable by EDS analysis.

Fig. 3a presents the temperature dependence of the electrical resistivity (ρ), as well as its error bars, for all $Ca_{0.97}Y_{0.01}La_{0.01}Yb_{0.01}Mn_{1-2x}Nb_xMo_xO_3$ samples. The estimation of the electrical resistivity error was 4% considering the sensitivity of the measuring system, and the inexactitude in the samples dimensions and the contacts distance, in agreement with previously published data [30]. As it can be observed in the graph, Nb, and Mo-free samples present the same metallic-like behaviour ($d\rho/dT > 0$) up to around 600 °C, and semiconducting-like one ($d\rho/dT < 0$) at higher temperatures. On the other hand, Nb, and Mo-doped samples display metallic-like behaviour ($d\rho/dT > 0$) in the whole measured temperature range. Furthermore, the electrical resistivity decreases on increasing the dopants content due to the enhancement of charge carrier concentration, in agreement with the results previously published results for B-site substituted manganites [31,32]. The substitution of Mn^{4+} with cations possessing a higher oxidation state, as Nb^{5+}, and Mo^{6+}, will introduce more electrons to the system and promote the formation of Mn^{3+} [32]. These modifications facilitate the electron hopping between Mn^{4+} and Mn^{3+}, which is the main mechanism for charge transport in manganites [33,34]. The lowest electrical resistivity at 800 °C (6.1 mΩ cm) was achieved in the highest doped materials, which is 60% lower than the obtained for Nd, and Mo-free samples. Moreover, as it can be observed from the data presented in Table 3, they are among the lowest values reported in the literature for materials prepared through longer processes.

The evolution of Seebeck coefficient and its errors with temperature, as a function of the sample composition, is plotted in Fig. 3b. About 4% error has been estimated for these measurements, which are influenced by the thermocouples error when measuring the temperature differences between the hot and cold sides of samples, as previously reported [30]. As it can be observed in the graph, the values are negative for all samples in the whole measured temperature range, confirming the n-type electronic conduction in these materials. Moreover, $|S|$ values of all samples increase when the temperature is raised. This evolution with temperature can be associated with that of a metal or a degenerate semiconductor when the carrier concentration, effective mass, and Fermi level are nearly constant with respect to temperature [50]. The highest $|S|$ value at 800 °C among the Nb, and Mo-doped samples has been achieved for $x = 0.005$ (210 μV/K). Even if this value is about 15% lower than the measured in Nb, and Mo-free samples, it is among the best reported in the literature, as shown in Table 3.

With the previous data of electrical resistivity and Seebeck coefficient, power factor variation with temperature, defined as $PF = S^2/\rho$, has been calculated for all samples (graph not presented). The highest PF value at 800 °C has been reached in $x = 0.01$ Nb, and Mo-substituted samples (~ 0.46 mW/K^{2}m) due to their better combination of both factors. This value is around 15% higher than the measured in Nb, and Mo-free samples. Furthermore, as illustrated in Table 3, it is among the highest reported in the literature.

Fig. 4a illustrates the evolution of total thermal conductivity with temperature determined for all samples, together with a 5% error, as it is the equipment accuracy stated by the manufacturer. As it can be observed in the graph, most of the samples present similar κ values in the whole measured temperature range, while it is higher for those with $x = 0.01$, and 0.03. On the other hand, all samples display similar behaviour with temperature, κ decreases up to around 600 °C, slightly increasing for higher temperatures. This evolution is due to the complex links between the different contributions to the total thermal conductivity. General decrease in the thermal conductivity with temperature is

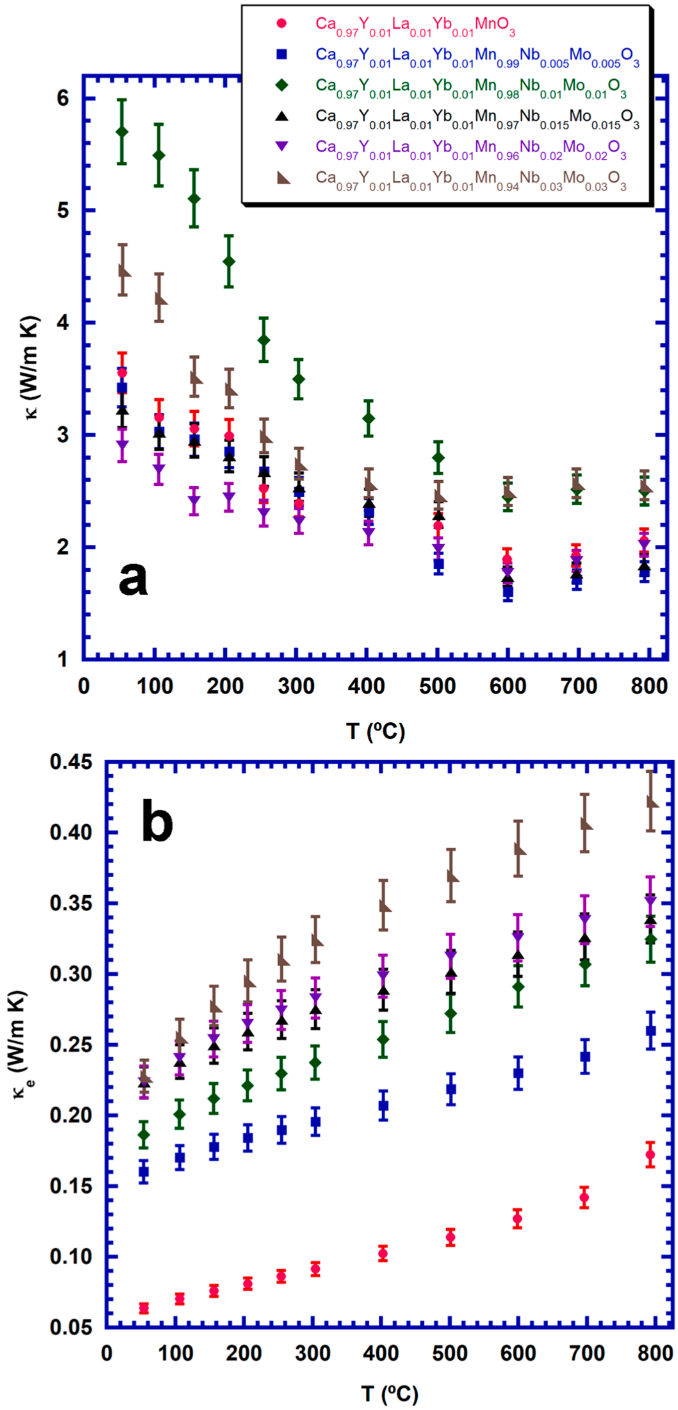

Fig. 4. Evolution with temperature of a) total thermal conductivity; and b) electronic thermal conductivity, together with their errors, for all samples.

a common behaviour for ceramic materials and is associated with the Umklapp phonon-phonon scattering (T^{-1}) [51]. The variation in thermal conductivity values for different compositions is particularly pronounced at lower temperatures. This is likely due to the effects of phonon scattering arising from microstructural differences and, to a lesser extent, from mass contrasts resulting from the substitution [51–53]. The increase in κ at elevated temperatures may be attributed to more intricate factors, such as a relaxation towards a more symmetrical crystal lattice, alterations in defect chemistry that do not substantially affect the charge transport, etc. The lowest thermal conductivity values at 800 ºC have been obtained in samples with x = 0.005, and 0.015 (~ 1.78 W/K m), which are only about 15% lower than the measured in Nb, and Mo-free samples. Moreover, as shown in Table 3, they are among the lowest ones typically reported for this family of materials. On the other hand, in spite of the increased contribution of the electronic thermal conductivity to the total one when the doping content, as shown in Fig. 4b, together with its 5% error, lattice thermal conductivity displays the same evolution observed for the total one in all cases.

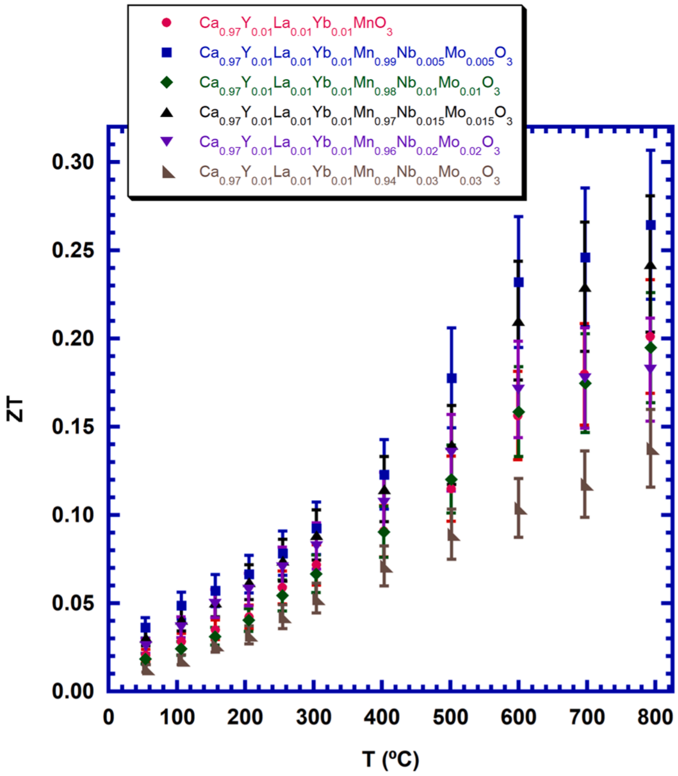

Fig. 5. Evolution of ZT and its errors with temperature for all samples.

In order to determine and compare the thermoelectric performances of the different materials, ZT evolution with temperature has been calculated using the Seebeck coefficient, electrical resistivity, and thermal conductivity data. These data are presented in Fig. 5, together with their errors, showing that the highest values have been achieved for x = 0.005 samples in the whole measured temperature range. This error has been calculated using the uncertainties of the physical parameters contributing to the dimensionless ZT. Taking these errors as 4% for the electrical resistivity and Seebeck coefficient, and 5% for the thermal conductivity, the error propagation principle leads to a maximum uncertainty of 16% for ZT values. Moreover, this error is in agreement with that previously reported (about 15%) [54]. The highest ZT value at 800 ºC reached ~ 0.27, which is about 30% higher than that obtained for Nb, and Mo-free samples prepared in this work, and it is one of the best reported in the literature in this family of materials, as it can be seen in Table 3.

All these characteristics, combined with an easily scalable preparation procedure make these materials promising candidates for their integration in high-temperature thermoelectric modules for power generation.

4. Conclusions

In this work, the use of multiple doping in the A-, and B-sites of $CaMnO_3$ has been studied. XRD patterns showed the formation of the thermoelectric phase as the major one in all cases, with very small amounts of $CaMn_2O_4$ secondary phase. Microstructural studies pointed out a slight decrease of grain sizes when the dopant content was increased. On the other hand, density measurements showed a slight increase with the dopant content. These modifications led to a significant drop in electrical resistivity with doping, reaching 6 mΩ cm at 800 ºC for x = 0.03 samples due to the increase in charge carrier concentration. As a consequence, the absolute Seebeck coefficient was decreased at the same time. The best power factor at 800 ºC has been found for x = 0.01 samples (~ 0.46 mW/K^{2}m), which is higher than the typically reported in the literature for this family of materials. The highest ZT value at 800 ºC has been achieved in x = 0.005 doped materials (~ 0.27), which is one of the best reported values for this family of materials, even taking into account the estimated error in the measurements. These properties, the high thermal stability of these manganite compounds, and the scalability of the preparation procedure make these materials very promising for large-scale production, targeting their use in thermoelectric modules for clean power generation.

CRediT authorship contribution statement

P. Amirkhizi: Samples preparation, Writing – original draft, Writing – review & editing. **O. J. Dura:** Thermal conductivity and density measurements, Writing – review & editing. **A. Kovalevski**: Resources, Writing – review & editing. **M. A. Torres:** Electrical resistivity, Seebeck coefficient, Writing – review & editing. **M. A. Madre:** Microstructural characterizations, Review & editing. **Sh. Rasekh**: Structural measurements, Writing – review & editing. **A. Sotelo:** Coordination, Evaluation of results, Writing – original draft.

Declaration of Competing Interest

The authors declare that they have no known competing financial interests or personal relationships that could have appeared to influence the work reported in this paper.

Acknowledgements

The authors wish to thank the Gobierno de Aragón (Grupo de Investigacion T54_23R) and Universidad de Zaragoza (UZ2022-IAR-09) for financial support. Sh. Rasekh acknowledges the support of the Research Employment Contract FCT-CEECIND/02608/2017. This work was also developed within the scope of the Ph.D project of P. Amirkhizi (grant 2020.08051. BD funded by FCT) and the project CICECO-Aveiro Institute of Materials, UIDB/50011/2020, UIDP/50011/2020 & LA/P/0006/2020, financed by national funds through the FCT/MCTES (PIDDAC). Authors would like to acknowledge the use of Servicio General de Apoyo a la Investigación-SAI, Universidad de Zaragoza.

References

[1] A.E. Risseh, H.P. Nee, O. Erlandsson, K. Brinkfeldt, A. Contet, F.F. Lng, G. Gaiser, A. Saramat, A. Saramat, T. Skare, S. Nee, J. Dellrud, Design of a thermoelectric generator for waste heat recovery application on a drivable heavy duty vehicle, SAE Int. J. Commer. Veh. 10 (2017) 26–44, https://doi.org/10.4271/2017-01-9178.

[2] L. Catalan, P. Alegria, M. Araiz, D. Astrain, Field test of a geothermal thermoelectric generator without moving parts on the Hot Dry Rock field of Timanfaya National Park, Appl. Therm. Eng. 222 (2023), 119843, https://doi.org/10.1016/j.applthermaleng.2022.119843.

[3] D.M. Rowe , 2006. In: D. M. Rowe (ed.), Thermoelectrics Handbook: Macro to Nano, 1st edn. CRC Press, Boca Raton, FL (USA).

[4] A.A. Yaroshevsky, Abundances of chemical elements in the earth's crust, Geochem. Int. 44 (2006) 48–55, https://doi.org/10.1134/S001670290601006X.

[5] S. LeBlanc, Thermoelectric generators: linking material properties and systems engineering for waste heat recovery applications, Sust. Mater. Technol. 1-2 (2014) 26–35, https://doi.org/10.1016/j.susmat.2014.11.002.

[6] I. Terasaki, Y. Sasago, K. Uchinokura, Large thermoelectric power in $NaCo_2O_4$ single crystals, Phys. Rev. B 56 (1997) 12685–12687, https://doi.org/10.1103/PhysRevB.56.R12685.

[7] D. Kenfaui, B. Lenoir, D. Chateigner, B. Ouladdiaf, M. Gomina, J.G. Noudem, Development of multilayer textured $Ca_3Co_4O_9$ materials for thermoelectric generators: Influence of the anisotropy on the transport properties, J. Eur. Ceram. Soc. 32 (2012) 2405–2414, https://doi.org/10.1016/j.jeurceramsoc.2012.03.022.

[8] J.G. Noudem, S. Lemonnier, M. Prevel, E.S. Reddy, E. Guilmeau, C. Goupil, Thermoelectric ceramics for generators, J. Eur. Ceram. Soc. 28 (2008) 41–48, https://doi.org/10.1016/j.jeurceramsoc.2007.05.012.

[9] T. Wang, P. Nan, H.C. Wang, W. Su, A. Sotelo, J. Zhai, X. Wang, Y. Ran, T. Chen, C. L. Wang, Right heterogeneous microstructure for achieving excellent thermoelectric performance in $Ca_{0.9}R_{0.1}MnO_{3\text{-}\delta}$ (R=Dy, Yb) ceramics, Inorg. Chem. 57 (2018) 9133–9141, https://doi.org/10.1021/acs.inorgchem.8b01163.

[10] D. Flahaut, T. Mihara, R. Funahashi, N. Nabeshima, K. Lee, H. Ohta, K. Koumoto, Thermoelectrical properties of A-site substituted $Ca_{1-x}Re_xMnO_3$ system, J. Appl. Phys. 100 (2006), 084911, https://doi.org/10.1063/1.2362922.

[11] Y. Wang, Y. Sui, W.H. Su, High temperature thermoelectric characteristics of $Ca_{0.9}R_{0.1}MnO_3$ (R = La, Pr, …,Yb), J. Appl. Phys. 104 (2008), 093703, https://doi.org/10.1063/1.3003065.

[12] E. Oz, S. Demirel, S. Altin, E. Altin, O. Baglayan, A. Bayri, S. Avci, Fabrication of Ca-Mn-Nb-O compounds and their structural, electrical, magnetic and thermoelectric properties, Mater. Res. Express 5 (2018), 036304, https://doi.org/10.1088/2053-1591/aab3af.

[13] A. Mishra, S. Bhattacharjee, Effect of A- or B-site doping of perovskite calcium manganite on structure, resistivity, and thermoelectric properties, J. Am. Ceram. Soc. 100 (2017) 4945–4953, https://doi.org/10.1111/jace.15015.

[14] X.Y. Huang, Y. Miyazaki, T. Kajitani, High temperature thermoelectric properties of $Ca_{1-x}Bi_xMn_{1-y}V_yO_{3-\delta}$ ($0 \leq x = y \leq 0.08$), Solid State Commun. 145 (2008) 132–136, https://doi.org/10.1016/j.ssc.2007.10.012.

[15] J.W. Park, D.H. Kwak, S.H. Yoon, S.C. Choi, Thermoelectric properties of Bi, Nb co-substituted $CaMnO_3$ at high temperature, J. Alloy. Compd. 487 (2009) 550–555, https://doi.org/10.1016/j.jallcom.2009.08.012.

[16] A. Sotelo, M.A. Madre, M.A. Torres, J.C. Diez, Effect of synthesis process on the densification, microstructure, and electrical properties of $Ca_{0.9}Yb_{0.1}MnO_3$ ceramics, Int. J. Appl. Ceram. Technol. 14 (2017) 1190–1196, https://doi.org/10.1111/ijac.12711.

[17] R. Lohnert, M. Stelter, J. Topfer, Evaluation of soft chemistry methods to synthesize Gd-doped $CaMnO_{3\text{-}\delta}$ with improved thermoelectric properties, Mater. Sci. Eng. B 223 (2017) 185–193, https://doi.org/10.1016/j.mseb.2017.06.014.

[18] R. Kabir, D. Wang, T. Zhang, R. Tian, R. Donelson, T.T. Tan, S. Li, Tunable thermoelectric properties of $Ca_{0.9}Yb_{0.1}MnO_3$ through controlling the particle size via ball mill processing, Ceram. Int. 40 (2014) 16701–16706, https://doi.org/10.1016/j.ceramint.2014.08.033.

[19] Y.-H. Zhu, W.-B. Su, J. Liu, Y.-C. Zhou, J. Li, X. Zhang, Y. Du, C.-L. Wang, Effects of Dy and Yb co-doping on thermoelectric properties of $CaMnO_3$ ceramics, Ceram. Int. 41 (2015) 1535–1539, https://doi.org/10.1016/j.ceramint.2014.09.089.

[20] M.A. Madre, H. Amaveda, O.J. Dura, D. Pelloquin, M. Mora, M.A. Torres, S. Marinel, A. Sotelo, Effect of Y, La, and Yb simultaneous doping on the thermal conductivity and thermoelectric performances of $CaMnO_3$ ceramics, J. Alloy. Compd. 954 (2023), 170201, https://doi.org/10.1016/j.jallcom.2023.170201.

[21] C. Oses, C. Toher, S. Curtarolo, High-entropy ceramics, Nat. Rev. Mater. 5 (2020) 295–309, https://doi.org/10.1038/s41578-019-0170-8.

[22] E. Heyn, Short reports from the metallurgical and metallographical laboratory of the Royal Mechanical and Technical Testing Institute of Charlottenburg, Metallographist 5 (1903) 39–64.

[23] K.R. Poeppelmeier, M.E. Leonowicz, J.C. Scanlon, J.M. Longo, W.B. Yelon, Structure determination of $CaMnO_3$ and $CaMnO_{2.5}$ by X-ray and neutron methods, J. Solid State Chem. 45 (1982) 71–79, https://doi.org/10.1016/0022-4596(82)90292-4.

[24] Q. Zhou, B.J. Kennedy, Thermal expansion and structure of orthorhombic $CaMnO_3$, J. Phys. Chem. Solids 67 (2006) 1595–1598, https://doi.org/10.1016/j.jpcs.2006.02.011.

[25] T. Roisnel, J. Rodriguez-Carvajal, 2023. WinPLOTR, a graphic tool for power diffraction, ⟨https://cdifx.univ-rennes1.fr/winplotr/winplotr.htm⟩. 15th, October, 2023.

[26] M.M. Gong, C.H. Chang, L.J. Wu, S. Dey, R.H.R. Castro, F. Liu, Modeling the grain growth kinetics of doped nearly fully dense nanocrystalline ceramics, Ceram. Int. 43 (2017) 6677–6683, https://doi.org/10.1016/j.ceramint.2017.02.062.

[27] A. Sotelo, M.A. Torres, M.A. Madre, J.C. Diez, Role of Ag on the properties of $Ca_{0.9}Yb_{0.1}MnO_3$ sintered ceramics, Materials 11 (2018) 2503, https://doi.org/10.3390/ma11122503.

[28] R. Kabir, R. Tian, T. Zhang, R. Donelson, T.T. Tan, S. Li, Role of Bi doping in thermoelectric properties of $CaMnO_3$, J. Alloy. Compd. 628 (2015) 347–351, https://doi.org/10.1016/j.jallcom.2014.12.141.

[29] H. Taguchi, T. Kugi, M. Kato, K. Hirota, Fabrication of $(Ca_{1-x}La_x)MnO_3$ ceramics with a high relative density and their power factor, J. Am. Ceram. Soc. 93 (2010) 3009–3011, https://doi.org/10.1111/j.1551-2916.2010.03987.x.

[30] M.A. Madre, F.M. Costa, N.M. Ferreira, S.I.R. Costa, Sh Rasekh, M.A. Torres, J. C. Diez, V.S. Amaral, J.S. Amaral, A. Sotelo, High thermoelectric performance in $Bi_{2-x}Pb_xBa_2Co_2O_y$ promoted by directional growth and annealing, J. Eur. Ceram. Soc. 36 (2016) 67–74.

[31] P. Kumar, S.C. Kashyap, V.K. Sharma, H.C. Gupta, Improved thermoelectric property of cation-substituted $CaMnO_3$, Chin. Phys. B 24 (2015), 098101, https://doi.org/10.1088/1674-1056/24/9/098101.

[32] C. Wang, L. Shi, X. Xu, S. Zhou, J. Zhao, Y. Guo, H. Liu, L. He, X. Cai, G. Xu, High-temperature thermoelectric characteristics of B-site substituted $Yb_{0.1}Ca_{0.9}Mn_{1-x}Nb_xO_3$ system ($0 \leq x \leq 0.1$), Appl. Phys. A 112 (2013) 1003–1009, https://doi.org/10.1007/S00339-012-7465-6.

[33] S.H. Chun, M.B. Salamon, Y. Lyanda-Geller, P.M. Goldbart, P.D. Han, Magnetotransport in manganites and the role of quantal phases: theory and experiment, Phys. Rev. Lett. 84 (2000) 757–760, https://doi.org/10.1103/PhysRevLett.84.757.

[34] G. Jakob, W. Westerburg, F. Martin, H. Adrian, Small-polaron transport in $La_{0.67}Ca_{0.33}MnO_3$ thin films, Phys. Rev. B 58 (1998) 14966–14970, https://doi.org/10.1103/PhysRevB.58.14966.

[35] N.M. Ferreira, N.R. Neves, M.C. Ferro, M.A. Torres, M.A. Madre, F.M. Costa, A. Sotelo, A.V. Kovalevsky, Growth rate effects on the thermoelectric performance of $CaMnO_3$-based ceramics, J. Eur. Ceram. Soc. 39 (2019) 4184–4188, https://doi.org/10.1016/j.jeurceramsoc.2019.06.011.

[36] M. Mouyane, B. Itaalit, Flash combustion synthesis of electron doped-$CaMnO_3$ thermoelectric oxides, Powder Technol. 264 (2014) 71–77, https://doi.org/10.1016/j.powtec.2014.05.022.

[37] Y.C. Zhou, C.L. Wang, W.B. Su, J. Liu, H.C. Wang, J.C. Li, Y. Li, J.Z. Zhai, Y. C. Zhang, L.M. Mei, Electrical properties of Dy^{3+}/Na^{+} Co-doped oxide thermoelectric $[Ca_{1-x}(Na_{1/2}Dy_{1/2})_x]MnO_3$ ceramics, J. Alloy. Compd. 680 (2016) 129–132, https://doi.org/10.1016/j.jallcom.2016.04.158.

[38] K.K. Liu, Z.Y. Liu, F.P. Zhang, J.X. Zhang, X.Y. Yang, J.W. Zhang, J.L. Shi, G. Ren, T.W. He, J.J. Duan, Improved thermoelectric performance in Pr and Sr Co-doped $CaMnO_3$ materials, J. Alloy. Compd. 808 (2019), 151476, https://doi.org/10.1016/j.jallcom.2019.07.188.

[39] M. Ohtaki, H. Koga, T. Tokunaga, K. Eguchi, H. Arai, Electrical transport properties and high-temperature thermoelectric performance of $(Ca_{0.9}M_{0.1})MnO_3$ (M= Y, La, Ce, Sm, In, Sn, Sb, Pb, Bi), J. Solid State Chem. 120 (1995) 105–111, https://doi.org/10.1006/jssc.1995.1384.

[40] G. Xu, R. Funahashi, I. Matsubara, M. Shikano, Y. Zhou, High-temperature thermoelectric properties of the $Ca_{1-x}Bi_xMnO_3$ system, J. Mater. Res. 17 (2002) 1092–1095, https://doi.org/10.1557/JMR.2002.0161.

[41] T. Chen, J. Wang, X. Wang, H. Wang, W. Su, J. Zhai, F. Mehmood, M. Khan, C. Wang, Cross-scale porous structure design leads to optimized thermoelectric performance and high output power for $CaMnO_3$ ceramics and their uni-leg modules, Appl. Mater. Today 29 (2022), 101557, https://doi.org/10.1016/j.apmt.2022.101557.

[42] Y. Wang, Y. Sui, H. Fan, X. Wang, W. Su, X. Liu, High temperature thermoelectric response of electron-doped $CaMnO_3$, Chem. Mater. 21 (2009) 4653–4660, https://doi.org/10.1021/cm901766y.

[43] A. Bhaskar, C. Liu, J. Yuan, Thermoelectric and magnetic properties of $Ca_{0.98}Re_{0.02}MnO_{3-\delta}$ (Re=Sm, Gd and Dy), J. Electron. Mater. 41 (2012) 2338–2344, https://doi.org/10.1007/s11664-012-2159-6.

[44] S.P. Singh, N. Kanas, T.D. Desissa, M.-A. Einarsrud, T. Norby, K. Wiik, Thermoelectric properties of non-stoichiometric $CaMnO_{3-\delta}$ composites formed by redox-activated exsolution, J. Eur. Ceram. Soc. 40 (2020) 1344–1351, https://doi.org/10.1016/j.jeurceramsoc.2019.11.027.

[45] D. Srivastava, F. Azough, R. Freer, E. Combe, R. Funahashi, D.M. Kepaptsoglou, Q. M. Ramasse, M. Molinari, S.R. Yeandel, J.D. Baran, S.C. Parker, Crystal structure and thermoelectric properties of Sr–Mo substituted $CaMnO_3$: a combined experimental and computational study, J. Mater. Chem. C. 3 (2015) 12245–12259, https://doi.org/10.1039/c5tc02318a.

[46] S.P. Singh, N. Kanas, M.-A. Einarsrud, Kjell Wiik, The effect of alkaline earth metal substitution on thermoelectric properties of $A_{0.98}La_{0.02}MnO_{3-\delta}$ (A = Ca, Ba), Process. Appl. Ceram. 16 (2022) 78–82, https://doi.org/10.2298/PAC2201078S.

[47] M. Molinari, D.A. Tompsett, S.C. Parker, F. Azough, R. Freer, Structural, electronic and thermoelectric behavior of $CaMnO_3$ and $CaMnO_{(3,\ -\delta)}$, J. Mater. Chem. A 2 (2014) 14109–14117, https://doi.org/10.1039/c4ta01514b.

[48] L. Bocher, M.H. Aguirre, D. Logvinovich, A. Shkabko, R. Robert, M. Trottmann, A. Weidenkaff, $CaMn_{1-x}Nb_xO_3$ ($x \leq 0.08$) perovskite-type phases as promising new high-temperature n-Type thermoelectric materials, Inorg. Chem. 47 (2008) 8077–8085, https://doi.org/10.1021/ic800463s.

[49] X. Song, S.A.P. Navia, L. Liang, C. Boyle, C.-O. Romo-De-La-Cruz, B. Jackson, A. Hinerman, M. Wilt, J. Prucz, Y. Chen, Grain boundary phase segregation for dramatic improvement of the thermoelectric performance of oxide ceramics, ACS Appl. Mater. Interfaces 10 (2018) 39018–39024, https://doi.org/10.1021/acsami.8b12710.

[50] D. Flahaut, J. Allouche, A. Sotelo, Sh Rasekh, M.A. Torres, M.A. Madre, J.C. Diez, Role of Ag in textured-annealed $Bi_2Ca_2Co_{1.7}O_x$ thermoelectric ceramic, Acta Mater. 102 (2016) 273–283, https://doi.org/10.1016/j.actamat.2015.09.036.

[51] E.S. Toberer, A. Zevalkink, G.J. Snyder, Phonon engineering through crystal chemistry, J. Mater. Chem. 21 (2011) 15843–15852, https://doi.org/10.1039/C1JM11754H.

[52] A.A. Yaremchenko, S. Populoh, S.G. Patrício, J. Macías, P. Thiel, D.P. Fagg, A. Weidenkaff, J.R. Frade, A.V. Kovalevsky, Boosting thermoelectric performance by controlled defect chemistry engineering in Ta-substituted strontium titanate, Chem. Mater. 27 (2015) 4995–5006, https://doi.org/10.1021/acs.chemmater.5b01389.

[53] H. Geng, X. Meng, H. Zhang, J. Zhang, Lattice thermal conductivity of filled skutterudites: an anharmonicity perspective, J. Appl. Phys. 116 (2014), 163503, https://doi.org/10.1063/1.4898686.

[54] S. Populoh, M.H. Aguirre, O.C. Brunko, K. Galazka, Y. Lu, A. Weidenkaff, High figure of merit in (Ti,Zr,Hf)NiSn half-Heusler alloys, Scr. Mater. 66 (2012) 1073–1076.